IOP Publishing Journal of Physics B: Atomic, Molecular and Optical Physics
J. Phys. B: At. Mol. Opt. Phys. **47** (2014) 185001 (8pp) doi:10.1088/0953-4075/47/18/185001

Helium-like titanium x-ray spectrum as a probe of QED computation

A T Payne[1], C T Chantler[1], M N Kinnane[1,2], J D Gillaspy[2], L T Hudson[2], L F Smale[1], A Henins[2], J A Kimpton[3] and E Takacs[4,5]

[1] School of Physics, The University of Melbourne, Australia
[2] National Institute of Standards and Technology, 100 Bureau Drive, Gaithersburg, MD 20899, USA
[3] Australian Synchrotron, Melbourne, Victoria 3000, Australia
[4] Department of Physics and Astronomy, Clemson University, Clemson, SC 29634, USA
[5] Experimental Physics Department, University of Debrecen, Debrecen, Bem tér 18/a, H-4026, Hungary

E-mail: chantler@unimelb.edu.au

Received 19 April 2014, revised 29 June 2014
Accepted for publication 28 July 2014
Published 28 August 2014

Abstract

We discuss the first absolute energy measurements of the intercombination and forbidden transitions (x, y, z) in trapped Ti^{20+} ions to 15 parts per million accuracy. We present new measurements on helium-like titanium, in which the orbital radius is reduced and QED terms are magnified by the increased nuclear charge. The measured transition energies are higher than predicted.

Keywords: helium-like, QED, x-ray spectroscopy, titanium, EBIT

(Some figures may appear in colour only in the online journal)

1. Introduction

Quantum electrodynamics (QED) is one of the most important foundations of modern physics. Recently there have been indications that the theory might be inconsistent with experimental findings. The five standard deviation inconsistency between a 15 ppm (parts per million) measurement of a muonic hydrogen transition and theory [1, 2] has led to four years of intensive research by many groups around the world. A similar inconsistency was raised in the 1998 reevaluation of the fundamental constants of nature [3], wherein the scattering data for the proton size was deemed inadequate within experimental uncertainties. The discrepancy was apparently resolved with improved QED and scattering calculations in the next round of evaluations [4], and a new value of the proton size was recommended based on all data. The large discrepancy in the muonic hydrogen measurement has once again brought into question the proton size, and perhaps QED itself [2]. The discrepancy of 0.42 meV seems well outside possible causes within the Standard Model, which are claimed to have an uncertainty of no more than ±0.01 meV [5]. Several complementary types of evidence exploring both the nuclear radius and QED spectroscopic discrepancies are summarized in figure 1 including the two-electron system of helium-like titanium, the subject of the present report. In the case of muonic hydrogen, the lepton orbital radius is reduced by the mass of the lepton, while in the case of highly charged ions the lepton orbital radius is decreased by the increased nuclear charge. While hydrogenic (one-electron) atomic systems represent critical challenges for theory and experiment, helium-like (He-like) atomic systems lie at one of the forefronts of QED research [6] because they display qualitatively new effects (including the 'two-electron Lamb shift') which are not present in one-electron ions.

Many QED contributions to atomic energy levels become dramatically larger for high atomic number along an isoelectronic sequence, but lie out of reach of laser techniques. Transitions which lie in the visible region for low-Z systems such as hydrogen become x-ray transitions when the atomic number Z is raised. Alternative theoretical approaches to QED yield different results testable with the precision realized in the present work [12].

This report tests QED by measuring transition wavelengths directly traceable to the length standard. The method is applied to He-like Ti, providing the first absolute measurements of the x, y and z transitions in this ion, and following on from an earlier significant study of the w transition [11]. Tests of QED in helium-like systems often observe the

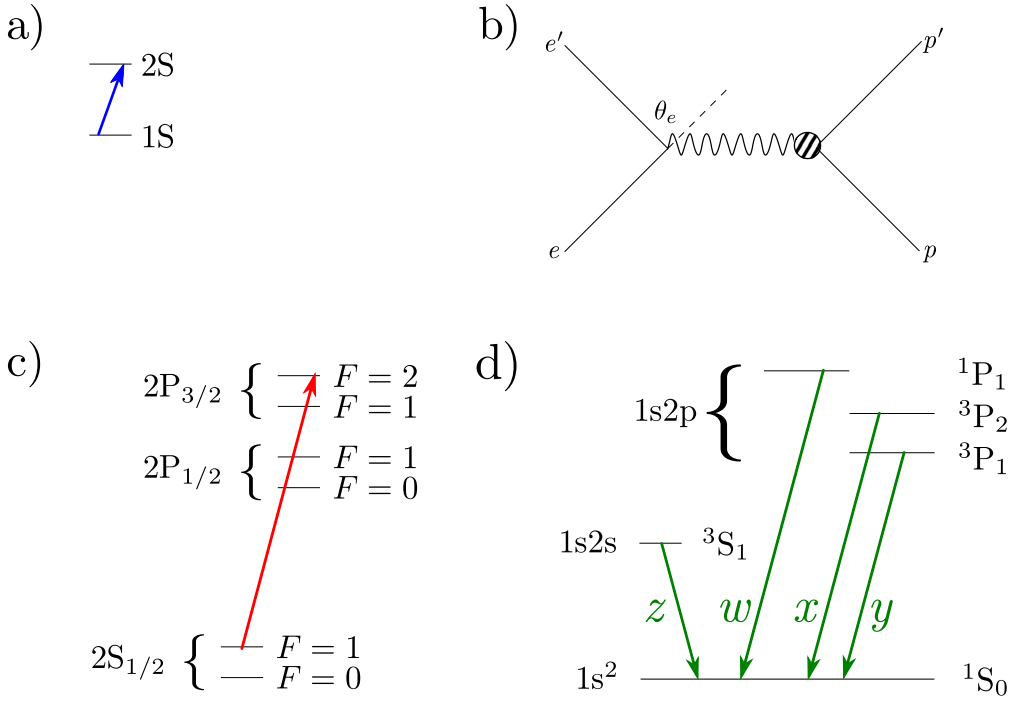

Figure 1. Experimental measurements exploring the discrepancy between QED formulations: (a) the 1S–2S transition frequency in atomic hydrogen [7]; (b) elastic electron–proton scattering [8–10]; (c) the $2S_{1/2}^{F=1}$–$2P_{3/2}^{F=2}$ Lamb shift in muonic hydrogen [1]; and (d) the absolute energy of the forbidden (z), resonance (w) and intercombination (x and y) transitions in helium-like ions [11]. Each of these experiments probe QED formulations, and motivate the improvement of theory.

x-ray diffraction profile of the high-intensity spectral lines from the $w(1s^2(^1S_0)\rightarrow 1s2p(^1P_1))$, and less frequently the x $(1s^2(^1S_0)\rightarrow 1s2p(^3P_2))$, $y(1s^2(^1S_0)\rightarrow 1s2p(^3P_1))$ and $z(1s^2(^1S_0)$ $\rightarrow 1s2s(^3S_1))$ transitions.

A key component of the method is the use of an array of ten calibration standards to tie the dispersion function of an x-ray spectrometer to the metre standard with high accuracy. A recent paper has provided evidence for a functional discrepancy of measurements of the helium-like w line from advanced QED theory [11].

Core shell transitions in medium-Z systems cannot be addressed by conventional lasers, so new techniques need to be developed, as discussed here. Efforts in medium-Z systems are limited by available x-ray calibration techniques (typically to 15 ppm or so), but can probe similar physics as the low-Z, UV-visible measurements due to the enhancement of contributions [13]. Here we find that this discrepancy also appears in a series of transitions (x, y, z in addition to w), strengthening the significance of our original finding and allowing the possible origin of the discrepancy in the upper or lower levels to be investigated by possible further theoretical work.

2. Experimental: EBIT

The EBIT [14] at the National Institute of Standards and Technology, Gaithersburg was used to provide highly charged titanium ions. A key advantage of EBITs is the monoenergetic electron beam which can be set to avoid dielectronic recombination resonances, thereby entirely avoiding the dominant source of satellite line shifts in high precision spectroscopic studies. Another advantage is the absence of Doppler shifts that often limited prior investigations with other sources.

In these experiments the nominal EBIT electron beam energy was set to 10 keV, selected to provide helium-like titanium ions in our case. Trapping and dumping cycle times with total cycle length of 400 ms, and trapping potentials of 200 V–500 V were tuned to maximize the population of helium-like titanium ions and minimize contaminating charge species. A metal vapour vacuum arc [15] was used to produce low charged titanium ions. Nitrogen is introduced to the trap to augment cooling. The trapped ion cloud axial dimension was about 20 mm with a typical electron beam diameter determining the radial extent of the excitation region of 66 μm. Hence the region of x-ray emission is a narrow cylinder in shape, and the detector position can be aligned to give high spectral resolution.

3. Experimental: Bragg diffraction

A Bragg diffraction Johann curved crystal spectrometer is used to collect x-ray spectra (figure 2). This spectrometer has a focusing effect which increases diffracted x-ray flux and minimizes the impact of variations in source location upon measured diffraction angles by over three orders of magnitude compared to flat crystal and von Hamos geometries [16, 17]. The curved crystal produces a circular focal plane (the

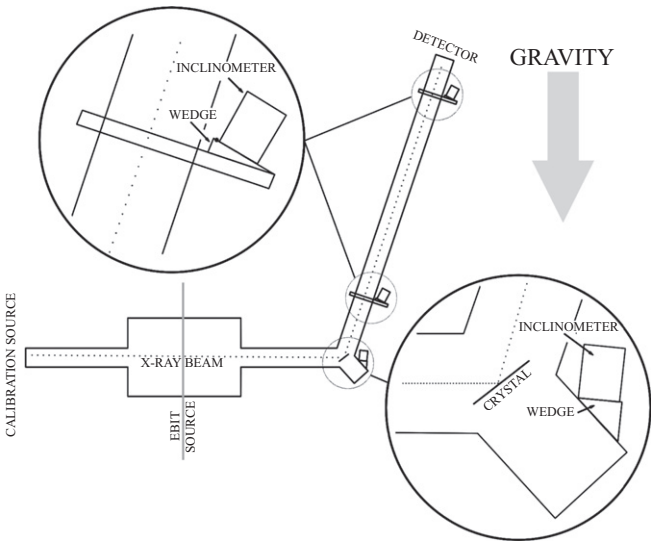

Figure 2. Diagram of the experimental setup showing the location of the gravity referenced inclinometers, the calibration and EBIT sources, and the detector on the Rowland circle. High accuracy x-ray diffraction is used to measure the detailed energy and profile of Bragg diffraction peaks arising from the *w, x, y* and *z* transitions of interest in the EBIT.

Rowland circle). Our spectrometer has a mechanical design that keeps the detector at the correct Bragg angle to collect diffracted photons *for all source energies* as the crystal is rotated relative to the source. Spectrometer angles are encoded using gravity-referenced inclinometers, allowing a variety of calibration lines to be used from a wide range of angles. Earlier work [16–19] demonstrated that a thorough understanding of diffraction conditions, dispersion relations and source systematics can allow the determination of transition energies in highly charged ions to a precision limited by statistics [12, 20]. Recent discussions of the history and developments of modelling code and diffraction support these advances [21–23], though the computation of dynamical diffraction penetration of wave fields into the diffracting crystal and the propagation of these profile shifts remains a challenging exercise for packages such as SHADOW, XOP, RAY and others. Together with spectrometer technology improvements, including suppression of spectrometer mechanical systematics, absolute broad energy range calibration and diffraction modelling, this has opened the door for high precision absolute x-ray wavelength measurements by reducing associated experimental uncertainties [24, 25].

Absolute determination of photon energy using Bragg diffraction requires precise determination of lattice parameter and photon diffraction angle. Absolute crystal lattice calibration and comparison of ideally prepared silicon is provided by x-ray optical interferometry (XROI) [26]. A lattice comparator is used to absolutely determine the crystal lattice parameter of silicon, germanium and related materials with the result directly traceable to the metre ($\delta - d$ [27]). For this work a Ge-220 cleaved crystal is used. Diffraction angle determination requires a function to convert measurable spectrometer angles to *absolute* photon diffraction angles. Reference peaks with energies defined by x-ray reference tables [28] are used as transfer standards from the work of XROI and $\delta - d$ to our curved germanium crystal planes, permitting the transfer of wavelength and angle on an absolute scale. While other work has used one or two such transfer points, a series such as we use here is necessary to identify and constrain systematics and the nonlinear dispersion function to the level required.

The diffracting crystal is a 0.8 mm thick germanium(220) crystal cut to the shape of an equilateral triangle with edge lengths of 25 mm. The crystal is curved by a two-bar crystal bender and mounted so that the crystal pole coincides with the rotation point of the crystal and detector arm. For the collection of the helium-like titanium results presented here the crystal is curved to a radius of 2.18 m which creates a Rowland circle focal plane with a radius of 1.09 m. The distance between the crystal and the EBIT is 663 mm ± 1 mm. The detector arm is a 1365 mm ± 2 mm long, 65 mm diameter, rigid tube and therefore the crystal to detector distance is fixed for all diffraction angles. In the Johann geometry, different diffraction angles correspond to different distances between the focal plane and diffracting crystal. The radius of curvature of the crystal is selected so that the detector centre intersects the Rowland circle at the angle of diffraction of the helium-like titanium, providing the highest resolution for the transitions being measured. The entire spectrometer is kept in vacuum at a residual pressure of 5×10^{-6} Torr (7×10^{-4} Pa) and isolated from the high vacuum environment of the EBIT by a 125 μm thick beryllium window.

The two-bar triangular crystal bender is stable over many years of operation and yields the ideal cylindrical curvature for the relevant crystal planes. The crystal curvature and perfection are measured by topography and interferometry, across the area of the crystal. The uniformity is tested by diffractometry to determine the dispersion function as discussed below, which is the most critical test.

4. Detector

The detector is a multi-wire gas proportional counter constructed and developed at The University of Melbourne [29–31]. A 33 mm diameter circular detector entrance window is covered by 250 μm thick beryllium. The interior of the detector is filled with an argon (90%) and methane (10%) gas mixture (P10). X-ray transmission through the entrance window increases from 86% to 90% over the calibration x-ray spectral range of 4–6 keV. The anode wire is maintained at +2150 V dc. A gas pressure of 1.25 atm is used to maximize detector efficiency while maintaining detector window integrity. CCD detectors of nominally higher resolution are often used in other work, but have significant variation of efficiency with energy and flux. Our detectors have demonstrated no significant loss of resolution while having high efficiency and the ability to tune efficiency with gas pressure and type over a suitable energy range.

5. Inclinometry

Crystal and detector angles are measured using a series of four independent gravity referenced inclinometers. The angle of an inclinometer is measured by the torque voltage of a pendulum with a *nominal* equation for converting voltage to angle given by $V_{\text{encoded}} = A_2 \times \sin(\Theta - A_0) - A_1$, where Θ is the angle of the unit to which the inclinometer is attached, A_0 is the intrinsic angular offset of the inclinometer, A_1 is the offset of the encoded voltage and A_2 is the conversion factor between angle and voltage. Each inclinometer used has characteristic parameters which are measured before and after experimental runs to verify temporal stability. The absolute accuracy of each inclinometer reading is ±0.005 V, at any angle, corresponding to sub-arcsecond accuracies in angle.

6. Calibration source

An electron fluorescence x-ray source is used to provide high-intensity characteristic x-rays. Scandium, titanium, vanadium, chromium and manganese target foils provide characteristic K transition energies (ten transitions of the form $K\alpha : 2p \rightarrow 1s$). The characteristic K transition diffraction angles from Ge-220 planes cover the spectrometer angular rotation range with manganese Kα at the high energy limit (smallest angle of diffraction), and scandium Kα at the low energy limit (largest angle of diffraction) (figure 2).

Characteristic K peaks of the calibration elements are asymmetric due to underlying atomic processes. An extensive investigation of Kα peak shapes was undertaken to provide a robust fitting routine [32] to accurately determine profile peak turning points. Kα spectra are fitted using the sum of six Voigt profiles. Centroid locations of Kα_1 and Kα_2 peaks, the absolute intensity of the Kα_1 peak, a common Gaussian width component representative of systematic broadening, and the Lorentzian width of the Kα_1 peak are left free, while all other parameters were constrained to known standard profile determinations [32]. Figure 3 shows a sample fit of vanadium Kα with underlying components. The electron gun spot size at the foil planes was 1.3 mm ± 0.2 mm. Electron beam energy was set to 20 keV for all calibration spectra.

7. Diffraction modelling

Diffraction angles are calculated using curved crystal diffraction modelling code [16, 17] to determine photon energy as a function of photon diffraction angle. Geometric input parameters for determination of the spectrometer dispersion function (crystal lattice parameter, crystal radius of curvature, length of illuminated crystal arc, calibration source to crystal distance, EBIT source to crystal distance, calibration and EBIT source sizes, detector to crystal distance) are taken from measurements of the apparatus prior to and during data collection. The dispersion curve has singularities on the Rowland circle, sensitive to experimental bandpass variations on and off the Rowland circle [16, 17]. Calibration source

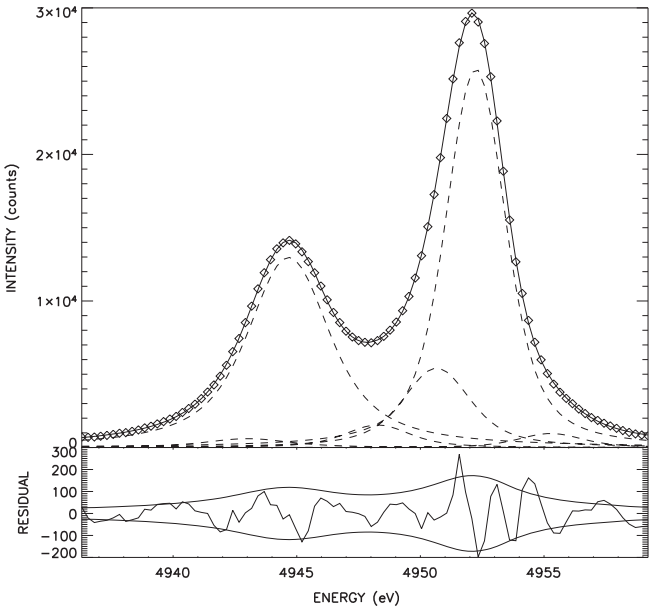

Figure 3. Vanadium Kα profile fitted using the high-accuracy methodology provided by [32], fitting the sum of six Voigts with common Gaussian broadening with defined constraints to metrological energies.

wavelength input parameters are taken directly from the work of Deslattes *et al* [28]. Profile peak turning points provide energy fiducials. Inclinometer calibration functions provide four independent measures of the detector arm angle from which a single angle is determined; for example of 41.1199° ± 0.0006° for the *w*-line. Close agreement between the predicted detector arm angles confirms good self-consistency between the calibration functions of inclinometers and instrumental settings. Final uncertainties in the helium-like titanium transition lines were dominated by uncertainty in fitted peak locations and the inclinometer determined spectrometer angle. Satellite contamination has been argued to be negligible [12].

We emphasize that we perform a calibration of the whole angular range of the spectrometer using multiple reference calibration lines. Both the ion cloud and the calibration sources are well within the Rowland Circle, as required to minimize the influence of source position on spectral response. Unlike flat crystal geometries, where micron translations of source and calibration have direct shift of interpreted positions, the curved crystal geometry is largely insensitive to this. In particular we have modelled such uncertainties as 1.5 mm in source to crystal distance, 20% uncertainty in source size and related possible systematics (see pp 115–300 [33]). In our geometry, these would produce a first-order shift of peak location on the detector of order (0.1–0.2) μm. The collection of similar systematics would lead to an uncertainty of (0.01–0.003) arc seconds in angle depending upon the configuration used in the experiment (and we used more than one), and these uncertainties correspond to an estimated (negligible) uncertainty of 0.06 ppm. Further, many of these shifts are cancelled in first order by the calibration procedure (see [33]).

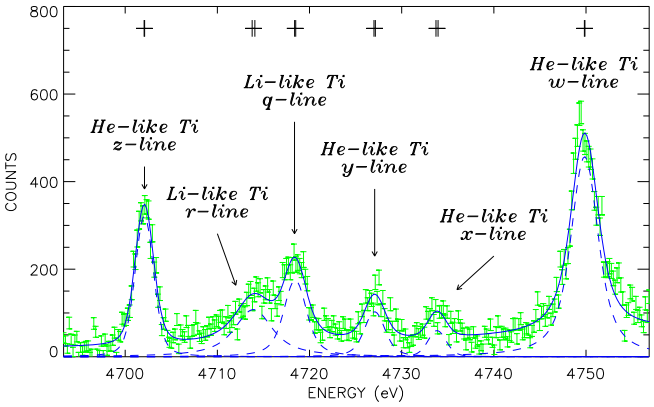

Figure 4. Experimental few-electron titanium spectrum from the EBIT plotted against energy. Raw data (green points with statistical standard error bars) with fitted individual peak profiles (blue dashed) and the full fit including the background (blue line). Centroid locations and uncertainties are shown above each peak as crosses. $\chi^2_r = 2.9$.

Hence we have uncertainties arising from the reference accuracy of the calibration lines and profiles; from the fits of the data collected from the calibration spectra; from the fits of the data collected from the gravity-referenced inclinometers; and from the overall fit of all of the dispersion function across the range of the spectrometer, and across the range of the detector face. Because the inconsistency of theoretical prediction in the actual geometry is represented as a variance whether due to errors or uncertainties in the calibration reference energy or profile, or in the fits and dispersion function, these uncertainties are included in table 1 in (i–vi) but these are actually dominated by the statistical uncertainty of the individual fits, rather than errors in the calibration reference or dispersion function modelling. In other words, the results are broadly consistent down to the statistical level.

By mapping the whole dispersion function across all angles of the spectrometer we tie down and remove all systematics relating to position offsets, focussing limitations, non-cylindrical curvature, off-axis saddle or spherical curvature, and even anomalous deviations of the calibration suite of characteristic lines tied to the metre. A great advantage of this procedure is that any errors or deviations from these or other sources are reflected in localized or general χ^2_r and variance of the combined data set. This is as opposed to approaches where a single characteristic line is used, or even two, when anomalous measurement can distort the derived values without an estimate of the systematic error associated with this. This is also as opposed to approaches which use no calibration line but assume a perfect cylindrical unstressed diffracting crystal with zero depth penetration of the quantum mechanical wave field into the crystal (which of course is non-physical).

8. Uncertainties

Figure 4 shows the fitted helium-like Ti spectrum. The six observed peaks correspond to the resonance lines the helium-like titanium *w*, lithium-like *r*, *q*, and helium-like titanium *x*, *y* and *z* transitions. The *w* line was analysed in a previous publication [11].

An experimentally determined detector background response function, quantified by calibration of the detector [29–31], is removed prior to the final peak fitting. The fitted function is the sum of six Voigt profiles with a quadratic background, with the instrumental Gaussian broadening common to all lines. Uncertainty is determined by the quadrature sum of contributions deriving from uncertainties in fitted spectral peak locations on the detector, tabulated standard wavelengths, the detector scale factor and inclinometer voltages from Gaussian peak widths.

The final data fit followed Levenberg–Marquardt least-squares analysis using six Voigt peaks, a common Gaussian width and a quadratic background function. Each data point was weighted as, $w_i = \left(y_i + X\right)^{-2}$ where y_i is the counting statistic and X represents the background noise observed from the quiescent detector. The *r*-line width was fixed at 20 channels as indicated by physics (this was a shallow correlated minimum due to the overlap of the *q* and *r* weak lithium-like contributions, but the lifetimes of these peaks are known to be similar). Comprehensive grid-searches were additionally performed over the fixed *r*-line width parameter and the constant background parameter *c*, to determine the impact of the uncertainty of each on final transition energies.

For an X shot noise of 100 with a one standard error (s.e.) range $X \in [64, 144]$ based on the noise analysis, an *r*-line width of 20±5 channels and all other fitting parameters free, the final fitted energies and 1 s.e. centroid uncertainties (σ_{centroid}) are listed in table 1. $\sigma_{\text{c-offset}}$ represents the uncertainty in transition energy due to the choice of background function.

Table 1 lists the uncertainty contributions of the final fit, with the calibration function uncertainty in the spectral region dominated by statistics. These uncertainties are summed in quadrature to give a total 1 s.e. uncertainty is 0.0720 eV for the *w*-line [11] and 0.0723 eV for the *z*-line. The final uncertainties on the *x* and *y* lines are dominated by statistics of the highly charged ion spectra rather than of calibration spectra, yielding uncertainties of 0.1311 eV and 0.1000 eV for the *x* and *y* lines respectively.

Taken individually, our measured helium-like transition energies demonstrate significant deviation from the most recent comprehensive *ab initio* theoretical QED formulation [6], with significances of 2.9 s.e. for the *w*-line, 1.4 s.e. for the *z*-line, and 1.3 s.e. and 0.3 s.e. for the *y*- and *x*-lines respectively. All lie higher than the predictions of theory. The weighted mean of our four deviations from theory (0.138 eV) is non-zero by 3.2 s.e.

The uncertainty in the dispersion calibration function was determined in two different ways, both of which agree very well. First, we estimate the various contributions to the uncertainty in the dispersion function separately (listed in the upper part of table 2). We could add them in quadrature, but this is not strictly correct, as some of the contributions may be mildly correlated and, of course, there could be unanticipated

Table 1. Transition energies with component and final uncertainties. The uncertainty in the absolute energy calibration function is contained within σ_{calib} and is dominated by calibration statistics including that of spectral line determination and clinometer (angle encoding) statistics following Levenberg–Marquardt least squares analysis [11]. The uncertainty in each w, x, y, z centroid (σ_{centroid}) represents the one-standard error (s.e.) centroid uncertainties arising from the fit of the spectral profile from the detector, also dominated by statistics. Additional minor components arise due to detailed investigation of the background function robustness $\sigma_{\text{c-offset}}$ and lithium-like r-line width $\sigma_{\text{r-width}}$. σ_{shot} is the uncertainty arising from the shot noise estimate from the data.

	Ti^{20+} LINE			
	w	x	y	z
E (eV)	4749.8520	4733.8335	4727.0667	4702.0782
E (eV) [6]	4749.6441	4733.8008	4726.9373	4701.9746
σ_{calib}	0.0650	0.0660	0.0660	0.0670
σ_{centroid}	0.0285	0.1128	0.0748	0.0267
$\sigma_{\text{c-offset}}$	0.0071	0.0096	0.0042	0.0047
$\sigma_{\text{r-width}}$	0.0034	0.0036	0.0010	0.0033
σ_{shot}	0.0089	0.0017	0.0051	0.0006
σ_{Total}	0.0720	0.1311	0.1000	0.0723
σ_{Total}/E (ppm)	15.15	27.69	21.15	15.39

Table 2. Sources contributing to the final uncertainty in E, presented specifically for the w transition. The dominant differences between transition accuracy lie in the statistical uncertainty of the centroid determination, as discussed in the main text. Components below the line are exactly as presented in the main fit. We expand component estimates (i–vi) for contributions to the dominant dispersion calibration function uncertainty, in terms of statistical and systematic components, which were determined directly but are consistent with a summation of components in quadrature. To this one-sigma uncertainty (i–vi) is added in quadrature uncertainties of the centroid fit of the spectrum, an uncertainty from constraining the width of the r component, an estimate of the uncertainty of the determination of the background, and an uncertainty in the estimation of the shot noise, to yield the total uncertainty in E_w.

Sources	Uncertainty (eV)	(ppm)
Statistical—EBIT Data Inclinometry Fit (i)	0.046	9.7
Statistical—Clinometry Calibration (ii)	0.035	7.3
Systematics—Detector Corrections (iii)	0.024	5.1
Systematics—Scale Factor (iv)	0.0026	0.54
Statistical—Detector Calibration Centroids (v)	0.0016	0.3
Systematics—Spectrometer Modelling (vi)	0.00033	0.07
σ_{calib} Dispersion Calibration Function (i-vi)	0.0650	14
σ_{centroid} Statistical—Detector Fit (vii)	0.0285	6
$\sigma_{\text{r-width}}$ Uncertainty-r—*Line Width* (viii)	0.0034	0.7
$\sigma_{\text{c-offset}}$ Background Uncertainty (*c*, etc) (ix)	0.0071	1.5
σ_{shot} Uncertainty in Shot noise (x)	0.0090	1.9
Total	0.0720	15.15

sources of additional error. Therefore, we independently estimate the total uncertainty in the dispersion function by recording the ten calibration lines under a variety of angles, and we examine the variance in each of the approximately 30 resulting spectral locations on the detector surface for some ten repeated measurement cycles (of order 300 spectra in total). The latter method gives a slightly (4%) larger uncertainty, which we use in table 2 for σ_{calib}.

In table 2 we present the summary for the w-transition, where we have deliberately expanded the dominant contribution to detail the component estimates of statistical and systematic contributions to the dispersion (energy) calibration. The two largest contributions (i and ii) are due to the statistical uncertainty in the clinometer readings which enter into the determination of the diffraction angles for both the x-ray calibration lines and the He-like Ti lines. The third largest contribution (vii) is due to the statistical uncertainty in the fit (figure 4). The dominant systematic presented is item (iii), the systematic uncertainty due to detector corrections, includes nonlinearities and channels/mm translational scale [30] which for all lines lies at 5.1 ppm. Further work will doubtless improve this. Systematic errors in the Ti spectral fit (iv, viii, ix, x) were estimated by an extensive investigation of the effect of changing the assumed form of the fit function, weights, and r-line width in the fit. Statistics relating to the centroid determinations of the calibration lines (v) and to the dynamical diffraction theory [16, 17] and functional form of the dispersion relation (vi) are minor.

9. Conclusions and outlook

Our earlier work [11] analyzed only the strongest of the four lines and included data from the literature up through the end of 2011, suggesting a systematic discrepancy from theory with a functional dependence proportional to Z^n. In that previous work [11], only integral coefficients were considered, since most QED terms can be expanded as integral powers of atomic number. The actual minimum occurred for the non-integer optimum of $Z^{3.5}$ [34]. The null hypothesis (that there is no discrepancy from latest theory, or that a constant offset from zero has an offset parameter of 0 eV) disagrees with a normally distributed dataset with a probability of 0.00003 [34]. The new results reported here are in very good agreement with the earlier data set to within uncertainty. This finding eliminates some possible sources of the observed discrepancy at $Z = 22$.

Techniques based on the refinement of the understanding of Bragg diffraction over the past several decades, coupled with the development of new methods of producing highly charged ions, currently enable the measurement of the x-ray spectra of highly charged ions to an accuracy of approximately 10 ppm. Bragg-based measurements at the 1 ppm level raise numerous systematic errors (corrections due to $n \geqslant 3$ satellites, depth penetration of wavefields, detector registration and curvature) that have not been adequately addressed in published results to date, and others of less well-defined magnitude for the case of highly charged ions excited by electron collisions (quantum interference shifts) [35, 36].

The significance of QED contributions increases with atomic number Z so that investigations at higher energies and atomic numbers are indicated. This can involve other diffracting crystals and crystal planes (e.g. Si 220, Ge 311) and can involve Laue spectrometers; but each of these would be a major undertaking with a multi-year schedule.

These results are the first set of measurements on He-like ions in which a comparison with theory has been undertaken with measurements across multiple spectral lines. All the observed transitions differ significantly, and in the same direction, from the most recent QED calculations. By observing and including several lines we limit the possibility of any asymmetry or line blends from impurities shifting one line in a particular direction.

Acknowledgments

We acknowledge J N Tan, J M Pomeroy and K Makonyi for contributions to general laboratory preparation and for participating in the operation and maintenance of the EBIT or ion injector during this experiment.

References

[1] Pohl R *et al* 2010 The size of the proton *Nature* **466** 213–7
[2] Antognini A *et al* 2013 Proton structure from the measurement of 2s-2p transition frequencies of muonic hydrogen *Science* **339** 417–20
[3] Mohr P J and Taylor B N 2000 CODATA recommended values of the fundamental physical constants: 1998 *Rev. Mod. Phys.* **72** 351–495
[4] Mohr P J and Taylor B N 2005 CODATA recommended values of the fundamental physical constants: 2002 *Rev. Mod. Phys.* **77** 1–107
[5] Jentschura U D 2011 *Ann. Phys., NY* **326**
[6] Artemyev A N, Shabaev V M, Yerokhin V A, Plunien G and Soff G 2005 QED calculation of the $n = 1$ and $n = 2$ energy levels in He-like ions *Phys. Rev.* A **71** 062104
[7] Parthey C G 2011 Improved measurement of the hydrogen 1S˜2S transition frequency *Phys. Rev. Lett.* **107** 203001
[8] Sick I 2003 On the rms-radius of the proton *Phys. Lett.* B **576** 62–67
[9] Blunden P G and Sick I 2005 Proton radii and two-photon exchange *Phys. Rev.* C **72** 057601
[10] Bernauer J C *et al* 2010 High-precision determination of the electric and magnetic form factors of the proton *Phys. Rev. Lett.* **105** 242001
[11] Chantler C T *et al* 2012 Testing three-body quantum electrodynamics with trapped ti^{20+} ions: evidence for a z-dependent divergence between experiment and calculation *Phys. Rev. Lett.* **109** 153001
[12] Chantler C T, Paterson D, Hudson L T, Serpa F G, Gillaspy J D and Takacs E 2000 Absolute measurement of the resonance lines in helium like vanadium on an electron-beam ion trap *Phys. Rev.* A **62** 042501
[13] Beiersdorfer P 2010 *J. Phys. B: At. Mol. Opt. Phys.* **43** 074032
[14] Gillaspy J D *et al* 1995 Overview of the electron-beam ion trap program at NIST *Phys. Scr.* **T59** 392–5
[15] Brown I and Washburn J 1987 The Mevva ion source for high current metal ion implantation *Nucl. Instrum. Methods Phys. Res.* **21** 201–4
[16] Chantler C T 1992 X-ray diffraction of bent crystals in Bragg geometry I perfect-crystal modelling *J. Appl. Crystallogr.* **25** 674–93
[17] Chantler C T 1992 X-ray diffraction of bent crystals in Bragg geometry II non-ideally imperfect crystals, modelling and results *J. Appl. Crystallogr.* **25** 694–713
[18] Chantler C T 1993 Photographic response to x-ray irradiation I: estimation of the photographic error statistic and development of analytic density–intensity equations *Appl. Opt.* **32** 2371–97
[19] Chantler C T, Laming J M, Dietrich D D, Hallett W A, McDonald R and Silver J D 2007 Hydrogenic Lamb shift in iron Fe25+ and fine-structure Lamb shift *Phys. Rev.* A **76** 042116
[20] Chantler C T, Paterson D, Hudson L T, Serpa F G, Gillaspy J D and Takacs E 1999 Precision x-ray spectroscopy at the NIST electron-beam ion trap: resolution of major systematic error *Phys. Scr.* **T80B** 440–2
[21] Authier A 2013 *X-Ray Standing Wave Technique: Principles and Applications* (Singapore: World Scientific) pp 36–7
[22] Als-Nielsen J 2008 X-rays and matter—the basic interactions *C. R. Phys.* **9** 479–86
[23] Uschmann I, Malgrange C and Forster E 1997 Measurement of a bent-crystal rocking curve with oscillations *J. Appl. Crystallogr.* **30** 1150–1
[24] Paterson D, Chantler C T, Tran C Q, Hudson L T, Serpa F G and Deslattes R D 1997 Absolute calibration of an x-ray spectrometer on the NIST electron-beam ion trap: control, design and systematics *Phys. Scr.* **T73** 400–2
[25] Gillaspy J D, Chantler C T, Patterson D, Hudson L T, Serpa F G and Takacs E 2010 First measurement of lyman alpha x-ray lines in hydrogen-like vanadium: results and implications for precision wavelength metrology and tests of QED *J. Phys. B: At. Mol. Opt. Phys.* **43** 074021
[26] Deslattes R D and Henins A 1973 X-ray to visible wavelength ratios *Phys. Rev. Lett.* **31** 972–5
[27] Kessler E G Jr, Owens S M, Henins A and Deslattes R D 1999 Silicon lattice comparisons related to the Avogadro project: uniformity of new material and surface preparation effects *IEEE Trans. Instrum. Meas.* **48** 221–4
[28] Deslattes R D, Kessler E G, Indelicato P, de Billy L, Lindroth E and Anton J 2003 X-ray transition energies: new approach to a comprehensive evaluation *Rev. Mod. Phys.* **75** 35–99
[29] Kinnane M N, Kimpton J A, de Jonge M D, Makonyi K and Chantler C T 2005 The correction of systematic image deformations inherent to two-dimensional proportional counters *Meas. Sci. Technol.* **16** 2280–6
[30] Payne A T, Kimpton J A, Kinnane M N and Chantler C T 2009 Simulation and minimization of nonlinear effects in backgammon-type multi-wire gas proportional counters *Meas. Sci. Technol.* **20** 025601
[31] Payne A T, Kimpton J A, Smale L F and Chantler C T 2010 Optimization of the spatial linearity in backgammon-type multi-wire gas proportional counters: the relevance of charge

cloud distribution *Nucl. Instrum. Methods Phys. Res.* A **619** 190–7

[32] Chantler C T, Kinnane M N, Su C H and Kimpton J A 2006 Characterization of Kalpha spectral profiles for vanadium, component redetermination for scandium, titanium, chromium, and manganese, and development of satellite structure for $Z = 21$ to $Z = 25$ *Phys. Rev.* A **73** 012508

[33] Kinnane M N 2009 Investigations of QED using precision spectroscopy of highly charged titanium ions *PhD Thesis* The University of Melbourne

[34] Chantler C T *et al* 2013 Testing three-body quantum electrodynamics with trapped ti^{20+} ions: evidence for a z-dependent divergence between experiment and calculation, reply *Phys. Rev. Lett.* **110** 159302

[35] Horbatsch M and Hessels E A 2010 Shifts from a distant neighboring resonance *Phys. Rev.* A **82** 052519

[36] Sansonetti C J, Simien C E, Gillaspy J D, Tan J N, Brewer S M, Brown R C, Wu S J and Porto J V 2011 Absolute transition frequencies and quantum interference in a frequency comb based measurement of the Li-6,Li-7 D lines *Phys. Rev. Lett.* **107** 259901